

# Classifying direct normal irradiance 1-minute temporal variability from spatial characteristics of geostationary satellite-based cloud observations

MARION SCHROEDTER-HOMSCHEIDT<sup>1\*</sup>, M. KOSMALE<sup>2,3</sup> and Y.-M. SAINT-DRENAN<sup>4</sup>

<sup>1</sup>Deutsches Zentrum für Luft- und Raumfahrt (DLR), Institut für Vernetzte Energiesysteme, Oldenburg, Germany

<sup>2</sup>Finnish Meteorological Institute (FMI), Arctic Space Centre, Helsinki, Finland

<sup>3</sup>Former affiliation: Deutsches Zentrum für Luft- und Raumfahrt (DLR) e.V., Deutsches Fernerkundungsdatenzentrum (DFD), Oberpfaffenhofen, Germany

<sup>4</sup>MINES ParisTech, PSL Research University, O.I.E. Centre Observation, Impacts, Energy, Sophia Antipolis, France

(Manuscript received September 6, 2019; in revised form March 9, 2020; accepted March 9, 2020)

## Abstract

Variability of solar surface irradiances in the 1-minute range is of interest especially for solar energy applications. Eight variability classes were previously defined for the 1 min resolved direct normal irradiance (DNI) variability inside an hour. In this study spatial structural parameters derived from satellite-based cloud observations are used as classifiers in order to detect the associated direct normal irradiance (DNI) variability class in a supervised classification scheme. A neighbourhood of  $3 \times 3$  to  $29 \times 29$  satellite pixels is evaluated to derive classifiers describing the actual cloud field better than just using a single satellite pixel at the location of the irradiance observation. These classifiers include cloud fraction in a window around the location of interest, number of cloud/cloud free changes in a binary cloud mask in this window, number of clouds, and a fractal box dimension of the cloud mask within the window. Furthermore, cloud physical parameters as cloud phase, cloud optical depth, and cloud top temperature are used as pixel-wise classifiers. A classification scheme is set up to search for the DNI variability class with a best agreement between these classifiers and the pre-existing knowledge on the characteristics of the cloud field within each variability class from the reference data base. Up to 55 % of all DNI variability class members are identified in the same class as in the reference data base. And up to 92 % cases are identified correctly if the neighbouring class is counted as success as well – the latter is a common approach in classifying natural structures showing no clear distinction between classes as in our case of temporal variability. Such a DNI variability classification method allows comparisons of different project sites in a statistical and automatic manner e.g. to quantify short-term variability impacts on solar power production. This approach is based on satellite-based cloud observations only and does not require any ground observations of the location of interest.

**Keywords:** Variability, global horizontal irradiance, direct irradiance, automatic classification, satellite-based, clouds, textural parameters

## 1 Introduction

Time series of surface solar irradiance are characterized by high variability on various scales. Obviously, there are seasonal cycles and daily extra-terrestrial cycles due to sun geometry. These are well known and can be described in a deterministic manner based on astronomical laws (e.g. IQBAL, 1983). The variability of cloud free (also called clear sky) irradiances at the earth's surface with respect to aerosol, water vapour, and atmospheric trace gas variations is described in clear sky models as e.g. the Copernicus Atmosphere Monitoring Service (CAMS) McClear model (LEFÉVRE et al., 2013; GSCHWIND et al., 2019). In general, the variability of irradiances caused by aerosols or water vapour

is small on time scales of minutes, while strong intra-hour variability results from extinction in clouds (e.g. SKARTVEIT and OLSETH, 1992 or TOVAR et al., 2001). Ramping events may even occur on time-scales as short as seconds (TOMSON, 2010; PEREZ et al., 2011; LAVE et al., 2012). For global irradiances, overshooting compared to clear sky irradiances or even to extra-terrestrial irradiances is observed as a result of three-dimensional scattering in clouds (SCHADE et al., 2007).

The introduction of the companion paper SCHROEDTER-HOMSCHEIDT et al. (2018) provides an overview on studies discussing the impact of fast fluctuations in surface solar irradiance for the solar energy sector. Overall, sub-hourly variability is an important issue for any coupled system of a solar energy system with storage as e.g. a battery. There is a general interest in obtaining correction factors to derive long-term time series of effective hourly irradiation as input to solar power models. Such correction factors depend on the respective solar

\*Corresponding author: Marion Schroedter-Homscheidt, Deutsches Zentrum für Luft- und Raumfahrt (DLR), Institut für Vernetzte Energiesysteme, Carl-von-Ossietzky-Str. 15, 26129 Oldenburg, Germany e-mail: marion.schroedter-homscheidt@dlr.de

energy technology as well as on individual use cases integrating solar energy into the energy supply chain. An automatic classification of minute-to-minute variability at any location of interest could serve as good basis in estimating correction factors for individual hours. A daily assessment of a variability status is not sufficient, as discussed e.g. by TOMSON (2010).

NOURI et al. (2019) are reporting that for solar power plant operations even knowledge of variability within one hour is not sufficient. They emphasize that variability should be monitored at least in 15 min intervals, which is basically possible with satellite imagery. Similar conclusions are expected for other online monitoring and control application as e.g. in electricity grid control.

Besides the temporal distribution, also spatial distribution of irradiance variability is important for electricity grid operations. Theoretical studies as e.g. ELSINGA et al. (2017) provide deterministic correlation functions versus distance or time for a group of single idealistically shaped clouds passing over photovoltaic systems. Nevertheless, realistic cloud fields are often multi-layered with strong geometrical variability. Several studies (e.g. KATO et al., 2011; HOFF and PEREZ, 2012; LAVE et al., 2012; or ANVARI et al., 2016) investigated spatial distributions of actually observed irradiance variabilities within ground-based pyranometer networks. They derived empirical parameterizations which can be applied for long-term statistics. Such an observational network with many instruments is technically very demanding and therefore hard to apply in daily operations over large spatial regions as requested in monitoring or for analysing the effects for a country or a continental region. Alternatively, a number of spatially distributed photovoltaic (PV) systems can be evaluated, but this approach provides information on generated power only and not solar radiation itself. Generated power is amongst others a function of individual PV-specific technical parameters and not directly a measure on solar radiation. These system parameters include orientation, size, technical efficiency and soiling state, as well as module temperature. Additionally, it requires initially the installation and metering of PV systems and does not provide the required information on radiation characteristics in a planning stage.

FERNANDEZ-PERUCHENA and BERNARDOS (2015) emphasize that the distribution of 1 min clearness index values depends significantly on local cloud characteristics. Satellite observations are providing on a global scale a good spatial as well as long-term temporal data coverage. That setting is offering information at any location of interest within the field of the view of the satellite. Furthermore, it allows the quantification of spatial distribution of irradiance variability compared to adjacent areas. As limiting factor, satellite-based observations from geostationary orbits are available only in temporal resolutions of 10, 15, 30, 60, or 180 min depending on the data period and region of the world. The operational Meteosat Second Generation Satellite (MSG) nowadays operates in a temporal resolution of 15 min.

Satellites as Himawari-8 (launched 2014) and GOES-16 (launched 2017) are providing 10 min and 15 min temporal resolution, respectively. Regional subsets of rapid scanning satellite observations are available every 5 min for Europe or the continental USA or 2.5 min for Japan, but these services are not available on a global scale and even may be re-focused depending on actual weather hazards. Therefore, it is currently impossible to directly derive statistical properties of a selected location from a satellite in higher temporal resolutions of one or few minutes. Note, that even with a potential 1 min resolving satellite observation mode the pixel size would still cover several square-km. The physical quantity measured by the satellite is thus a spatial average, where high frequency fluctuations present in the 1 min ground measurements are smoothed out.

Since direct point observations of irradiances on 1 min basis are not available from current satellites, there is still the need performing an indirect satellite evaluation to derive the 1 min variability status. Having developed such an automated analysis offers then the opportunity to use the already existing long-term observation datasets from satellites and take advantage of their global coverage. PEREZ et al. (2011) showed that temporal variability metrics based on clearness index increments can be statistically estimated from the clearness index at the time of the hourly satellite observation and a spatial variability measure of clearness indices in the surrounding  $3 \times 3$  pixels. This spatial area corresponds to a  $30 \times 30$  km<sup>2</sup> area. This conclusion was found for various intervals of e.g. 20 sec, 1 min, 5 min, or 15 min but also a dependency of the statistically best fit from the chosen geographical location was found.

HINKELMAN et al. (2013) show that 1 min GHI ramps as observed by ground-based observations are related to different cumulative distribution functions for varying cloud types. In their study, cloud types were separated into fog, water phase, super-cooled, opaque, and thin cirrus clouds as detected from GOES satellite-based observations. The structure of this dependency is comparable at all stations investigated in the United States. Hinkelman's work underlines the approach of our study that local and regional weather patterns observed by satellites can be classified automatically and as follow up contribute to typical irradiance variability classes. In a similar work, RENO and STEIN (2013) quantify hourly variability of 1 min GHI ramp rates of ground-based time series in relation to cloud types classified from GOES satellite imagery. These cloud types according to the NOAA GOES Surface and Insolation Product (GSIP) discriminate between clear, partly cloudy/fog, water cloud, super-cooled/mixed phase cloud, optically thick ice cloud, optically thin ice cloud, and finally multi-layered clouds which correspond to cirrus above lower level clouds. Even these cloud type classifications of both papers differ in its level of detail while both schemes are based on multi-spectral satellite observations and classification on individual pixel level. The study presented here is going beyond this approach,

as it couples similar multi-spectral cloud retrievals for neighbouring pixels into spatial features derived from the cloud mask. Such an approach allows an automatic assessment of overall meteorological cloud patterns on the mesoscale range towards a DNI variability assessment.

In the companion paper [SCHROEDTER-HOMSCHIEDT et al. \(2018\)](#) and based on the underlying master thesis [JUNG \(2015\)](#), a reference data base of single hours using 1 min resolved ground observations was created. These individual hours were divided in eight DNI variability classes comprising information on high to low ramping in DNI as well as high to low clear sky index. Clear sky index is defined as ratio of observed irradiance to a cloud-free case and can be seen as a measure of the energy provided in the hour. The individual classes are defined to describe different impacts on ground-based radiation due to cloud cover and cloud features. In [SCHROEDTER-HOMSCHIEDT et al. \(2018\)](#) this database is used to derive a supervised DNI variability classification for 1 min resolved ground-based DNI time series. By using the same reference data base as training set, this paper investigates hourly and 15 min resolved satellite-based observations of clouds and their spatial structures to derive DNI variability class information.

Combining spectral and textural features was already widely used in cloud remote sensing for detecting clouds in satellite imagery (e.g. [EBERT, 1987](#) or [GARAND, 1988](#)). Using multi-pixel satellite information to implement cloud type classification was used in the past for nowcasting natural hazards, such as thunderstorms affecting air traffic (as summarized and presented in an own approach by [BERENDES et al., 2008](#)) or in [JAKOB and TSELIODIS \(2003\)](#) for global climate model development. Irradiance variability patterns from 15 min resolved spectral and textural features were classified by [JUNG \(2015\)](#) and for spatially higher resolved, but only once or twice per day available polar orbiting satellites, by [WATANABE et al. \(2016\)](#). The work presented in the current paper elaborates the approach presented by [JUNG \(2015\)](#).

Section 2 shortly describes the reference data base as well as the satellite-based cloud observations and derived spatial structure parameters. Section 3 provides the description of the automatic classification scheme and its validation. Example results at various stations are provided and discussed in Section 4. Section 5 finally concludes the paper.

## 2 Data

### 2.1 Reference database of DNI variability classes

This study uses a reference data base for eight irradiance variability classes with different variability structures in 1 min resolved GHI and DNI time series. These already classified hours with different variability conditions were derived based on a visual classification

of 1 min DNI ground observations by three independent experts and derived as the training basis for a supervised variability classification for DNI time series ([SCHROEDTER-HOMSCHIEDT et al., 2018](#)). The data base aims at classifying 1 min resolved variability within one hour by using generic irradiance variability classes. It consists of 300 cases in total and is distributed with number of cases for each class ranging from 16 to 54. It was provided as a supplement in [SCHROEDTER-HOMSCHIEDT et al. \(2018\)](#).

The reference data base was derived from observations between 9 and 14 UTC in 2012 at the Baseline Surface Radiation Network (BSRN, [OHMURA et al., 1998](#)) station Carpentras in Southern France. Hours with transitions between two irradiance variability classes were excluded to provide a useful training dataset. The BSRN station Carpentras was chosen due to its location relevant for the solar energy sector. It is affected by a large variety of clouds and DNI variability patterns as it is affected both by typical Mediterranean and Central European climates whereas it is neither a mountainous nor a coastal station showing only specific cloud features. It is therefore assumed that these selected variability classes also serve as generic and universal classes at other locations.

[Fig. 1](#) illustrates the variability classes with respect to DNI. Black curves provide the 10 min running mean DNI while yellow curves provide the 1 min resolved DNI ground observation. Red boxes mark the hours selected as part of the reference database for each variability class. Please note that only a few hours of each day are selected as other hours are either affected by low sun conditions, show another variability class or are transition hours with changing variability conditions inside the hour. Our previous studies ([GLAS, 2014](#)) have shown that a classification of days into variability classes as e.g. done by [KANG and TAM \(2013\)](#) or [RAUSCHER \(2013\)](#) is not justified due to frequent changes in variability conditions during the day. This was further confirmed e.g. by [NOURI et al. \(2019\)](#) who even claim the usage of a 15 min variability classification as necessity for some applications as short-term forecasting in concentrated solar power plants.

The variability classes were extensively described in [SCHROEDTER-HOMSCHIEDT et al. \(2018\)](#) with respect to clear sky index and variability parameters derived from 1 min resolved ground-based irradiance observations. Annex A in [SCHROEDTER-HOMSCHIEDT et al. \(2018\)](#) provides a visualisation of all reference database members. The variability classes are sorted from large to small  $k_{cDNI}$ . The clear sky index  $k_c$  is defined as ratio between actually measured GHI and theoretically expected GHI in the cloud free case, which is taking only Rayleigh scattering, trace gas absorption, and aerosol extinction into account. The beam clear sky index  $k_{cDNI}$  is built in a similar manner as ratio between DNI and cloud free DNI.

[Fig. 2](#) presents the relative frequency clear sky index  $k_c$  and  $k_{cDNI}$  increments together with cumulative

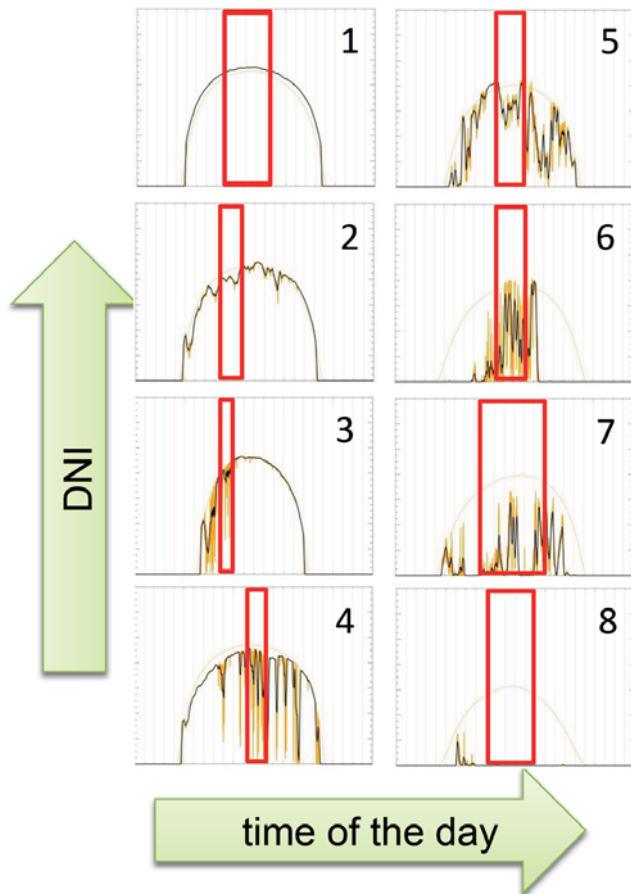


**Figure 1:** Examples of the variability classes 1 to 8 as used in the reference database. Hours being classified into one of the classes are marked by a red box. Minute resolved DNI values (yellow), 10 min DNI moving averages (black) and clear sky DNI values (thin) are given (taken from SCHROEDTER-HOMSCHIEDT et al., 2018, their Fig. 5).

density of fractional GHI and DNI changes to quantify ramps. The relative frequency is defined as the number of occurrences of  $k_c$  values in histogram boxes with a defined width of 0.1 and divided by the maximum frequency of each individual class. Furthermore, cumulative distributions are provided for fractional GHI and DNI changes, which are minute-wise absolute ramp rates normalized by  $1000 \text{ W/m}^2$  and given as percentage.

Frequency distributions of  $k_c$  and  $k_{cDNI}$  increments differ remarkably between DNI variability classes. Classes 4 and 6 have largest minute-by-minute increments and slowly increasing cumulative distributions, while differing mainly by their mean  $k_c$  of 0.89 and 0.77 and mean  $k_{cDNI}$  of 0.79 and 0.48, respectively. Classes 1, 2, and 8 have a small width of relative frequency distributions and steeper increase in cumulative distributions. Class 3 shows larger tails of large increments than classes 5 and 7 and a smaller increase in the range of large absolute ramps in the cumulative distributions. Both patterns for the GHI and DNI are structurally similar as expected but differ in the extreme values as DNI

is more sensitive to clouds and higher variable as it can reach zero values while GHI always is above zero during daytime due to the diffuse radiation component.

## 2.2 Ground-based observations

This study uses ground-based measurements from the Baseline Surface Radiation Network (BSRN, OHMURA et al., 1998). BSRN stations provide GHI, DNI, as well as diffuse sky irradiance in 1 min temporal resolution. The data base is quality controlled following the procedures described in LONG and DUTTON (2012). BSRN stations Cabauw (The Netherlands), Camborne (UK), Carpentras (France), Izana (Spain), Payerne (Switzerland), Sariguen/CENER (Spain), Sede Boker (Israel) are used below as well as DLR's PSA (Spain) station.

Furthermore, all classification results are compared also to ground measurements as obtained in the EnerMENA network (SCHÜLER et al., 2016). This includes EnerMENA stations Adrar (Algeria), Cairo (Egypt), Erfoud (Morocco), Missouri (Morocco), Oujda (Morocco), TanTan (Morocco), and Zagora (Morocco).

The stations are chosen since they are located in different climate zones and provide data for the selected reference year 2012. Finally, they are all located within Meteosat Second Generation satellite's field of view.

## 2.3 Satellite-based cloud parameters

The APOLLO (AVHRR Processing scheme Over cLOUDs LAND and OCEAN; KRIEBEL et al., 1989; SAUNDERS and KRIEBEL, 1988; KRIEBEL et al., 2003) methodology delivers cloud mask, cloud type, cloud optical depth, and cloud top temperature as cloud physical parameters for all fully cloudy MSG (Meteosat Second Generation) SEVIRI (Spinning Enhanced Visible and InfraRed Imager) pixels.

The temporal resolution is 15 min during daytime and data is available since 1<sup>st</sup> February 2004. Pixel size is  $3 \times 3 \text{ km}^2$  at satellite nadir and increases to  $4 \times 5$  or  $5 \times 6 \text{ km}^2$  towards the mid-latitudes. MSG's 15 min operating mode is available for more than 10 years now, while other satellite services do not cover longer time series so far. Therefore, this study focuses on the field of view of MSG.

From APOLLO cloud retrievals, a number of pixel-wise classifiers is used. Furthermore, a group of classifiers is suggested which uses the information in a window around the pixel of interest.

### 2.3.1 Pixel-wise classifiers

Fully and partly cloudy pixels are discriminated. Cloud coverage as the fraction inside a pixel covered by a cloud, expressed in percent, is derived for each altitude level and thin clouds separately. Cloud coverage is calculated at daytime by analysing the dependency between reflectance measured at  $0.6 \mu\text{m}$  and  $0.8 \mu\text{m}$  with average reflectances for fully covered and cloud-free pixels

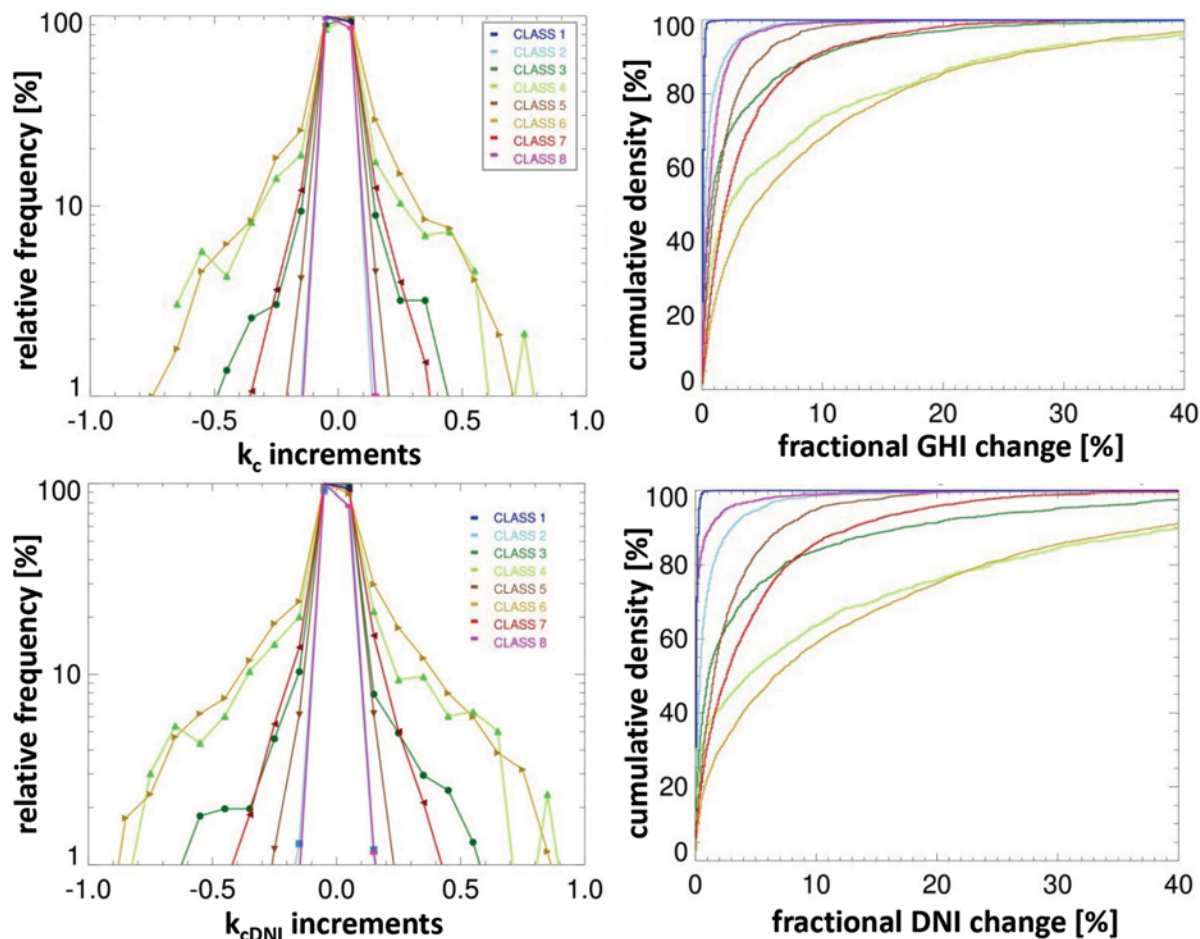


**Figure 2:** Relative frequency of minute-by-minute  $k_c$  and  $k_{cDNI}$  increments for all eight variability classes (left) and cumulative distributions of absolute GHI and DNI ramp rates normalized with  $1000 \text{ W/m}^2$  (right).

in a surrounding box of  $58 \times 58$  pixels. This size of the surrounding box was defined in the 1980ies and it differs from the later found surrounding boxes of  $3 \times 3$  and  $29 \times 29$  pixels for the spatial features in Section 2.3.2. This is accepted as the APOLLO cloud retrievals are obtained from the operational CAMS radiation service input dataset which cannot easily be changed.

The cloud type discriminates between low-level, medium-level, and high-level reaching water or mixed-phase clouds and high-level thin ice clouds. It is derived using cloud phase, cloud top temperature, and a comparison against the standard vertical temperature profiles. The layer boundaries are set to 700 hPa and 400 hPa with the associated temperatures taken from standard atmospheres. The thin cloud layer exclusively contains thin pure ice phase clouds with no thick clouds underneath. For partially cloudy pixels the cloud type is assigned as the most frequent cloud type in a  $58 \times 58$  pixel environment. Literally defined cloud types clear, thin ice, low, medium, and high-level clouds are set to 0, 1, 2, 3, and 4 as numerical values according to increasing impact on solar surface radiation.

Cloud optical depth is derived in a first step only for fully cloudy pixels. A post-processor is applied to estimate  $\tau_{\text{cloud}}$  for partly cloudy pixels. The estimated

optical depth of the partly covered pixel is computed firstly by taking the average of all  $\tau_{\text{cloud}}$  of the fully covered pixels of same type of cloud in this region, and then by multiplying this average by the cloud coverage inside the pixel.

### 2.3.2 Spatial features as classifiers

Beside features derived from multispectral satellite observations for each individual satellite pixel only, also spatial features describing the relationship of neighbouring pixels in either a close neighbourhood of  $3 \times 3$  or a wider neighbourhood of  $29 \times 29$  pixels are applied (Fig. 3). The selection of  $3 \times 3$  pixels is motivated by their characteristic of being direct neighbours. The selection of  $29 \times 29$  pixels is justified by optimized classification results presented later. Such features have also been called textural features in remote sensing literature before.

Fig. 3 qualitatively illustrates how different scattered or overcast clouds look from the satellite point of view. Visually, differences between the four satellite images on the upper left of Fig. 3 are obvious, but it is not straight forward to detect different cloud situations automatically and to assess them with respect to variability

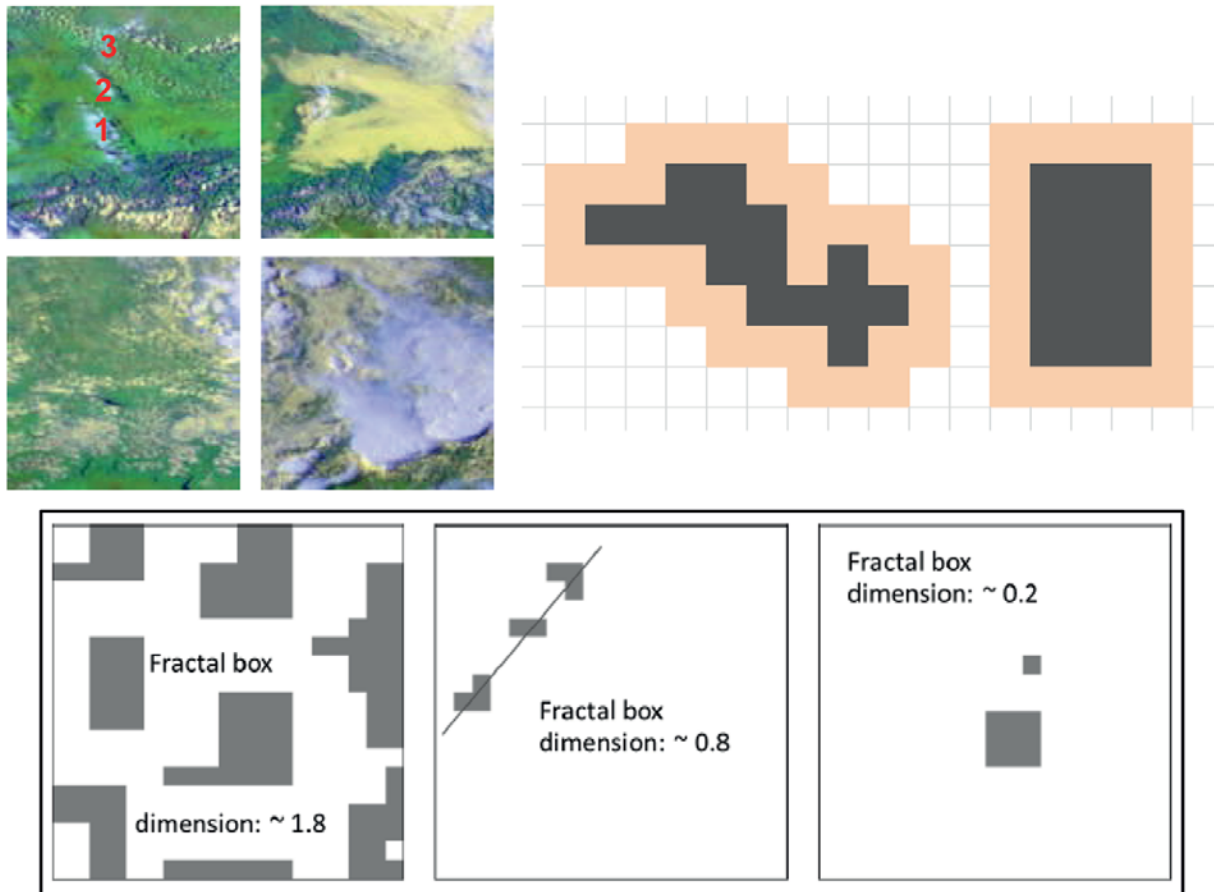


**Figure 3:** Schematic illustration of spatial features used as classifiers. Example satellite images illustrate the variability of cloud situations and the classifier ‘number of clouds’ representing spatially connected areas in the cloud field (upper left), the number of cloud/cloud free changes in the neighbourhood marked in orange (upper right), and examples of typical values of the fractal box dimension (lowest row).

in radiation at the surface. This study is a suggestion for such a quantitative and automatic approach.

Cloud fraction in the window is derived as the ratio of all pixels being detected as cloudy and all pixels existing in the window. Partially cloudy pixels are weighted with their individual cloud fraction.

The number of clouds is obtained by using an 8-neighbour search strategy using all horizontal, vertical, and diagonal neighbours within a binary cloud mask in order to identify cloud structures. Fig. 3 (upper left) illustrates how spatially connected areas of cloudy pixels are counted as a single cloud by marking 3 clouds as examples.

The number of cloud/cloud free changes among pixels within the window is calculated from the binary cloud mask. It sums the adjacent cloud free pixels in the neighbourhood of a cloud. In Fig. 3 (upper right) they are marked in orange. Cloud/cloud free changes are counted for each column and each row first separately and summed up as the final number of cloud/cloud free changes in the cloud mask.

Clouds can be described as fractal objects down to a size of approx. 350 m as shown by BEYER et al. (1994). This was analysed for sky camera observations with a pixel size of 7 m and by PIETRAPERTOSA et al. (2001) for

high resolution satellite-based observations with a pixel size of 16 m. MAAFI and HARROUNI (2003) applied the fractal approach to classify daily GHI time series into cloudy, partly cloudy, and clear sky conditions. In our study, the fractal box dimension is used as an additional classifier representing the fractal characteristic of the cloud field. Artificial example cloud fields and their typical fractal box dimensions are illustrated in Fig. 3 (lower panel). The fractal box dimension in a window is calculated as a box-counting dimension as used in CARVALHO and SILVA DIAS (1998).

Overall the cloud compactness can be summarized by typical values found for box dimension and the number of cloud elements (Table 1).

The cloud area type is finally a parameter describing the nearby 3×3 pixel neighbourhood of the central pixel. The decision tree is presented in Fig. 4. It was derived by analysing many situations during the reference years. Thresholds are arbitrarily chosen from examples and checked in many other cases visually.

In case the satellite pixel is partly cloudy or cloud free, cloud area type is set to ‘clear’ if the cloud fraction is below 30 %; to ‘scattered’ if the cloud fraction is between 30 and 80 %; and to ‘broken/overcast’ if the cloud fraction is above 80 %. If the pixel is fully cloudy,

**Table 1:** Typical values of box dimension and number of clouds for different cloud compactness cases.

Fractal box dimension	Nb of cloud elements	Cloud compactness
2	1	Overcast
1.7 to 1.9	$\leq 5$	Few large clouds
1.8 to 2	$> 5$	Broken clouds
0 to 1.7	$\leq 5$	Isolated clouds
0.5 to 1.8	$> 5$	Scattered clouds

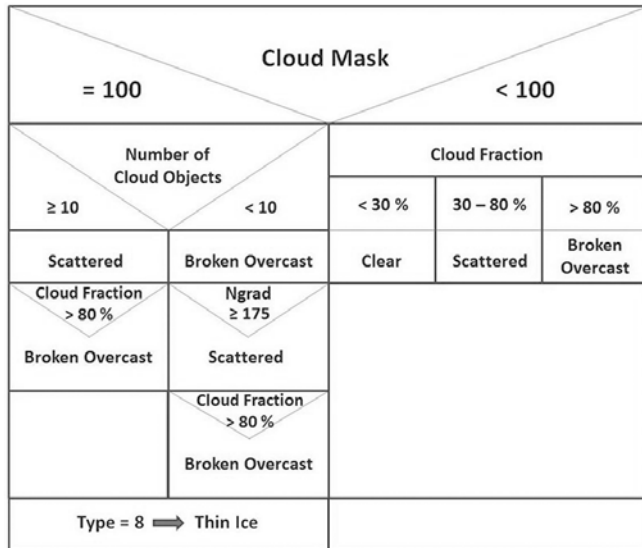


**Figure 4:** Scheme to derive the cloud area type describing the nearby neighbourhood of a pixel. Cloud fraction is defined here as cloud fraction in a 3x3 pixel window.

the number of clouds in the surroundings is evaluated. If the number of clouds is above 10 then the situation is classified as ‘scattered’ unless the pixel’s cloud fraction is above 80% which points to a ‘broken/overcast’ situation in the pixel and its nearby surroundings. If there are only few clouds (less than 10) in the surroundings, the situation is classified as ‘broken/overcast’ unless there are more than 175 cloud/cloud-free changes in the 29x29 window which results in a classification as ‘scattered’. The number of 175 was derived empirically from visual assessment of many satellite images. The latter selection may again be overwritten by the very local conditions inside the pixel if the pixel’s cloud fraction is above 80%. In case the cloud type at the pixel location was identified as thin ice cloud, this overwrites all previous findings with the cloud area type ‘thinIce’. In a final step the occurrence of cloud/cloud free changes between the centre pixel and its direct neighbours is checked – if they exist, the cloud area type is set back to scattered, as local effects are expected to dominate such cases. The literally defined classes ‘none’, ‘clear’, ‘scattered’, ‘broken/overcast’, and ‘thin ice’ are coded as numerical values 0, 1, 2, 3, and 4 in the classification process.

### 3 Automatic classification

#### 3.1 Irradiance variability classes described by satellite-based classifiers

In this paper the irradiance variability classes are described with respect to satellite-based classifiers related to all pixel and window-based cloud parameters (Table 2 to 4).

The cloud type at a satellite pixel is typically clear for classes 1 to 4 and includes typically thin cirrus for

**Table 2:** Hourly irradiance variability class characterisation by pixel-wise parameters cloud type, cloud optical depth, and cloud coverage. All median values and the P25 and P75 range (in brackets) are given.

Class	cloud type [-]	cod [-]	coverage [%]
1	0 (0, 0)	0.0 (0.0, 0.0)	0 (0, 0)
2	0 (0, 0)	0.0 (0.0, 0.0)	0 (0, 0)
3	0 (0, 0)	0.0 (0.0, 0.0)	0 (0, 0)
4	0 (0, 2)	0.0 (0.0, 0.0)	0 (0, 1)
5	1 (0, 1)	0.4 (0.0, 0.4)	1 (0, 10)
6	1 (0, 2)	0.9 (0.0, 2.9)	16 (0, 56)
7	2 (1, 3)	2.0 (0.4, 3.3)	40 (13, 100)
8	3 (3, 4)	22.1 (13.9, 28.5)	100 (100, 100)

**Table 3:** Hourly irradiance variability class characterisation by window-based parameters fractal box dimension, number of clouds, and number of cloud/cloud free changes. All median values and the P25 and P75 range (in brackets) are given.

Class	boxdim [-]	num. of clouds [-]	num. of cloud/cloud free changes [-]
1	1.14 (0.93, 1.31)	1 (0, 5)	6 (0, 38)
2	1.55 (1.30, 1.75)	4 (2, 6)	94 (27, 136)
3	1.74 (1.65, 1.85)	5 (4, 6)	154 (101, 173)
4	1.79 (1.65, 1.84)	7 (4, 8)	137 (115, 236)
5	1.83 (1.73, 1.95)	4 (1, 6)	146 (75, 183)
6	1.96 (1.83, 1.97)	2 (1, 4)	121 (72, 170)
7	1.97 (1.97, 1.97)	1 (1, 1)	9 (0, 64)
8	1.97 (1.97, 1.97)	1 (1, 1)	0 (0, 0)

**Table 4:** Hourly irradiance variability class characterisation by further window-based parameters cloud fraction in window and cloud area type. All median values and the P25 and P75 range (in brackets) are given. Additionally, the number of cases in the reference database is given.

Class	cloud area type [-]	cloud fraction in window [%]	num. of cases [-]
1	‘none’	0 (0, 2)	54
2	‘none’	2 (1, 14)	35
3	‘none’	17 (9, 28)	23
4	‘scattered’	22 (10, 28)	16
5	‘clear’	14 (9, 27)	39
6	‘scattered’	42 (21, 55)	51
7	‘scattered’	60 (43, 72)	42
8	‘broken/overcast’	94 (87, 98)	38

classes 5 and 6. Low level clouds are dominating class 7 and medium and high level optically thick clouds are dominating class 8. Statistics of cloud optical depth shows that classes 5 to 7 have low COD classes with P75 values around COD of 3 and P90 values of up to 10. In classes 1 to 4, the COD at pixel location is often zero. Nevertheless, classes 2, 3, and 4 show some variability of direct irradiances even if the COD in the pixel itself is zero. This may have various reasons: (a) cirrus clouds may be sub-visible in the satellite pixel of several square km size, (b) local cumulus clouds may affect a neighbouring pixel in a parallax effect as a function of cloud height, sun position, and satellite geometry; and (c) small scale, but optically thick clouds may be overlooked in the satellite pixel. Therefore, cloud information from the surrounding box is useful to discriminate between classes 1 to 4 and their smaller scale variations which may be overlooked by the satellite physical retrieval inside the individual, best geo-located pixel either due to spatial resolution or parallax effects.

The fractal box dimension in the 29×29 pixel window increases systematically from classes 1 to 6 and remains constant for classes 7 and 8 where the value of 1.97 occurs as an upper limit. The theoretical value of 2 is not reached. This is caused by applying the fractal box dimension algorithm on a restricted 29×29 pixel area only, instead of an indefinite spatial area. The number of clouds in the surrounding box is largest for classes 2, 3, 4, and 5, while there are only fewer clouds in the surroundings for classes 1, 6, 7, and 8.

For the number of cloud/cloud free changes, the classes 3, 4, 5, and 6 show maximum values. It may be noted that class 6 has a low number of clouds but a large number of changes between cloud and cloud free pixels. This represents few larger clouds with many gaps and a very rough border in the 2-dimensional cloud mask as seen by the satellite. The cloud area type ‘broken-Overcast’ dominates class 8 and can be found in the P75 of class 7 but does not occur in all other classes within the P25 to P75 interval. Scattered clouds are dominating classes 4, 6, and 7 while class 5 is typically represented by a clear cloud area type. The window cloud fraction also increases with class number – with exception of class 5, which has a median cloud fraction of 14 %. The P25 and P75 values in classes 3, 4, and 5 are very similar, but the median value varies between 17, 22, and 14 %.

A corresponding assessment can be made for the 15 min resolved classification using the full temporal resolution of the satellite data. The average cloud coverage in class 6 increases from 16 to 21 % and in class 7 from 40 to 47 %. The fractal box dimension in clear sky classes decreases from 1.14 to 1.05 representing more isolated or scattered clouds which are more visible if only a single snapshot satellite image is used instead of averaging 4 consecutive satellite images. Also, the fractal box dimension’s P25 percentiles for classes 2 and 3 are decreasing from 1.3 to 1.24 and from 1.65 to 1.57. All other parameters change only gradually and non-systematically.

### 3.2 Automatic classification scheme

Based on the cloud parameters introduced as classifiers in Section 2, the typical values of all classifiers are derived and given as Box-Whisker representation showing the median as well as P25 and P75 percentiles for each cloud parameter (Fig. 5). The distributions are derived for all hours in the reference database. All indices are scaled to a range of 0 to 1.5 for better visualization. The classifier values are far from being constant for individual classes, but compared to the other variability classes, the distributions of values within one variability class differ systematically for most classes. Classes 3 and 4 differ less systematically than the remaining classes and may therefore be difficult to distinguish with satellite observations. Nevertheless, these difficult classes 3 and 4 are still considered in the analysis to account for consistency with classification results obtained from ground-based observations as presented in [SCHROEDTER-HOMSCHIEDT et al. \(2018\)](#) and [NOURI et al. \(2019\)](#).

The dependencies between the classifiers are evaluated first visually by using scatterplots of each classifier against each other classifier. There were no redundant classifiers found. Furthermore, the dependency was further quantified by using Pearson correlation coefficients for an assessment of the reference data set. Correlation heat maps for all classes are evaluated – individually for each class and aggregated over all classes (Fig. 6). An individual correlation heat map for a single class typically results in a few entries with high correlation values close to 1 – indicating that two classifiers are redundant for this variability class. But doing so for all eight variability classes, no systematic overall redundancy is found. This is quantified further by calculating the sum of the correlation coefficient over all classes. The sum of correlation would reach 8 in case of any two classifiers being duplicative. Maximum correlation sum values reach the value of 6. Therefore, it is meaningful to keep all classifiers as they represent different parts of the observed irradiance variability.

Class 1 is characterized by lowest fractal box dimensions, a small number of clouds and cloud/cloud free changes inside the window, as well as by a low window cloud fraction. Both cloud type and cloud area type classifiers are indicated as clear for all cases. The fractal box dimension increases with class number until it reaches its maximum in full cloud coverage classes 7 and 8. The number of clouds and number of cloud/cloud free changes is largest for the high variability class 4. The window cloud fraction shows small and rather similar values for classes 1, 2 and then again for classes 3, 4, and 5, before it increases to full cloud coverage in class 8.

It is remarkable that classes 1 to 4 do not differ in the single-pixel-only classifiers as cloud type, cloud optical depth, and cloud coverage. Single-pixel-only classifiers are only suited to discriminate classes 5, 6, 7, and 8 while the window-related classifiers fractal box dimen-

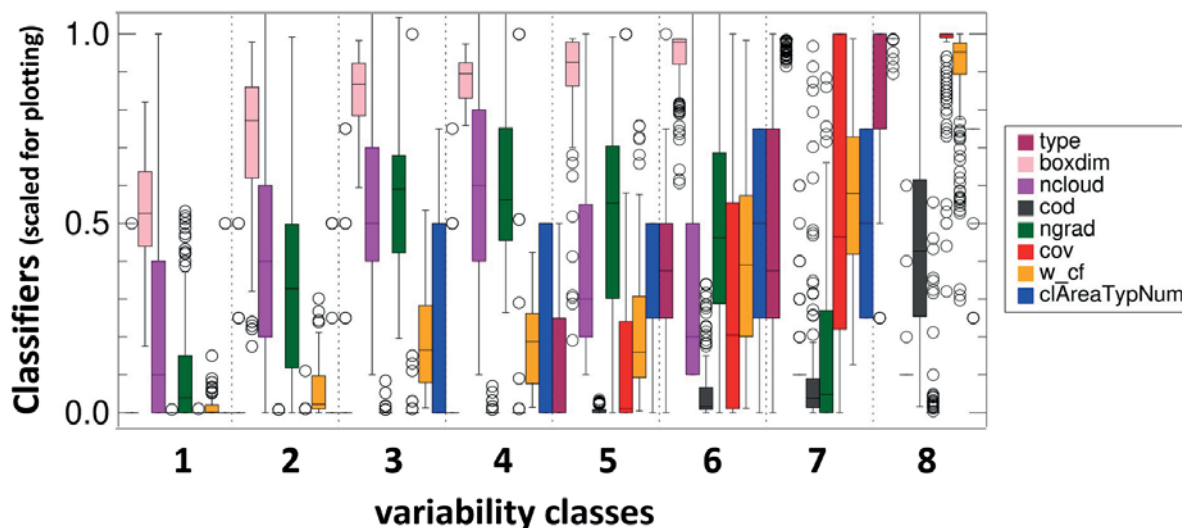


**Figure 5:** Box-Whisker plots for each satellite-based classifier (scaled for easier visualization) and for each irradiance variability class. Median values are given as black lines within each box. The box itself reaches from the lower to the upper quartile. The whiskers represent the maximum values in the distribution that are less than 1.5 times the inter quartile distance away from the median. Further outliers are marked as circles.

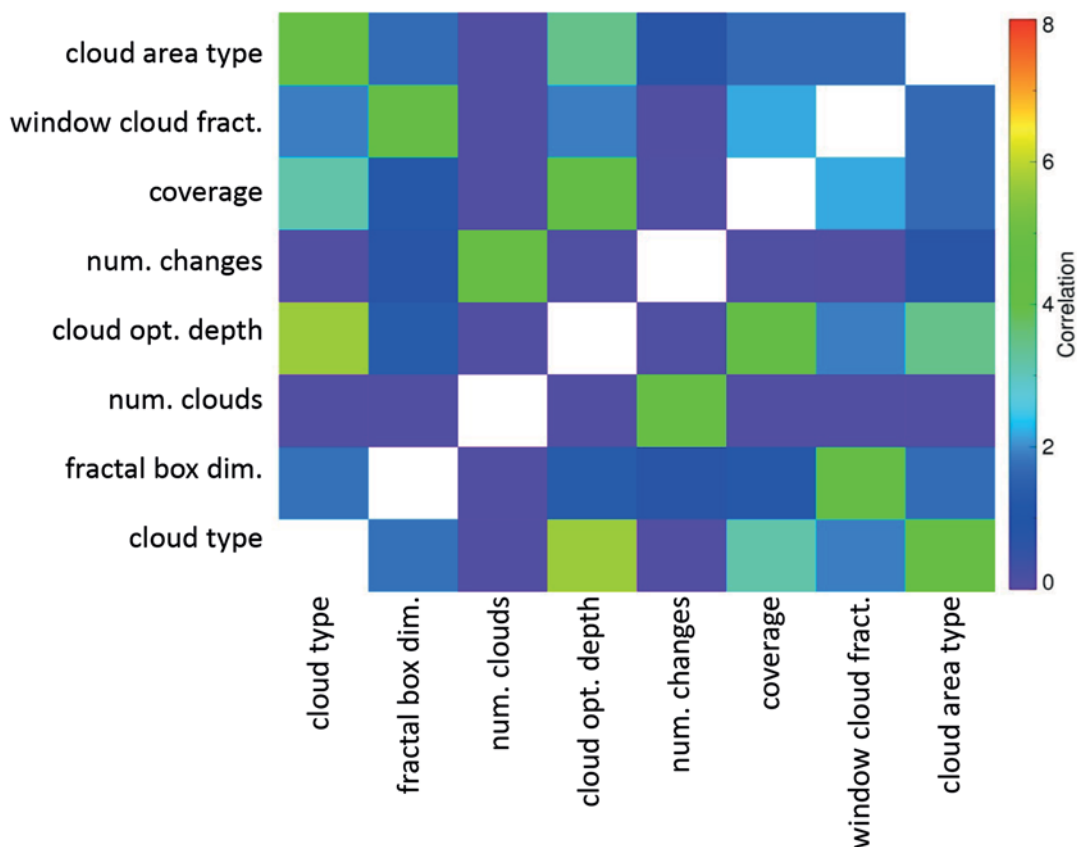


**Figure 6:** Aggregated correlation heat map for all satellite-based predictors as sum over all 8 classes. Autocorrelation values on the diagonal are not shown.

sion is better suited to discriminate classes 1 to 5. The same applies to the window-related classifier ‘number of clouds’ which only helps to classify classes 1 to 6 but does not discriminate classes 7 and 8 anymore. The more sensitive window-based classifier of cloud/cloud

free changes as well as the window cloud fraction are well suited to discriminate the full range of classes but are less sensitive to discriminate classes 3 and 4 from each other. Finally, the cloud area type is relevant to distinguish classes 5 to 8. Per definition this parameter is

for many cases closely related to the neighbourhood of the centre pixel and therefore tends to behave similar as the single-pixel-only classifiers.

All above described cloud parameter distributions are used in the automatic, supervised classification scheme as ‘reference distributions’. All classifiers are treated in a similar way: For each satellite observation the distance between the classifier value for the actual satellite image towards the median of the reference distribution is calculated. This is repeated for each variability class and summed up for all classifiers. The class with the lowest distance sum is claimed as result for this satellite observation and for the location of interest which is the central pixel inside the window.

In general, the automatic classification is performed every 15 min for each image provided by the satellite. This is advantageous and needed in user applications as e.g. shown by [NOURI et al. \(2019\)](#). Nevertheless, the reference database was set up on an hourly basis, since daily classifications were found to be not sufficient (e.g. [TOMSON, 2010](#)). In order to compare automatic, satellite-based classification results versus the visually selected and controlled reference data base, hourly mean automatic classification results are needed. They are derived as the mean of four quarter-hourly values available during each hour.

### 3.3 Comparing the satellite-based and the reference classification

For validation the automatic classification scheme is applied to all hours in the reference database (Fig. 7). The distributions for all classes peak on or next the 1:1 line. Overall, 55 % of all hours are placed into the same class by using the satellite-based compared to the manual expert-based classification scheme. Hit rate in the satellite-based classification are 70, 37, 48, 50, 51, 31, 60, 92 % for classes 1 to 8, respectively. There are two groups of classes – class 2 and 6 with low detectability and the other classes with higher detectability.

This is very much in line with results of [WATANABE et al. \(2016\)](#) who found average classification results of 56 and 61 % for two classification methods and a similar spread of results in their 6 variability classes. They used MODIS 1 km resolved cloud classifiers, which were averaged over  $45 \times 45 \text{ km}^2$  and compared against 2-hourly temporal windows with 1 min resolved global horizontal irradiances. Their result was obtained from the one or two overpass times of the MODIS instrument on board the polar orbiting satellites AQUA and TERRA and using ground observations from Japan.

These results are better than those found in a similar classification exercise based on artificial neural networks as discussed in [SCHRECK \(2018\)](#). The neural network approach used the same reference dataset as labelled dataset and the same cloud predictors, but achieved only a classification result of 40 % due to a very flat probability function for the intermediate variability classes as result of the neural network.

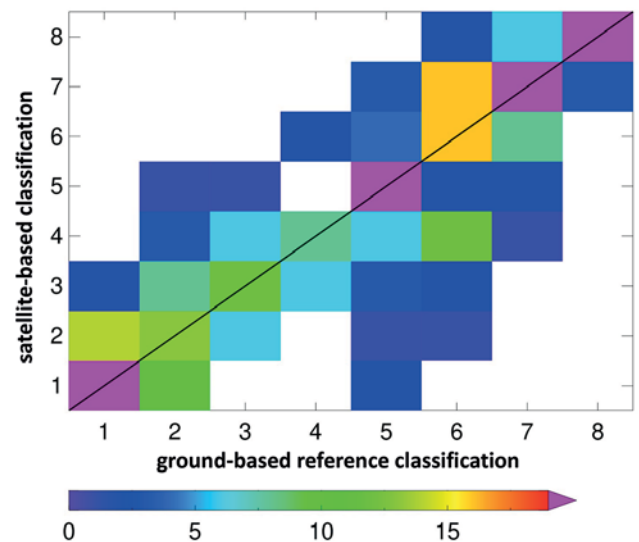


**Figure 7:** Density scatter plot for the satellite-based classification versus the ground-based reference classification.

Since a visually based definition of variability classes in the reference database is somewhat arbitrary in transition zones between two classes, a second evaluation is made by counting the classification into a neighbouring class as a success. Following [BORG et al. \(2011\)](#) it is recommended to assess any automatic classification in comparison to an expert-based classification. In our case neighbouring classes are classes with consecutive class numbers, but also classes 4 and 6 which are similar in their characteristics. Applying these assumptions, the detection rate is 92 %. This strong improvement in classification accuracy illustrates the fact that, gross classification errors are seldom and that in far most of the cases, variability situations being close to each other are misclassified. For real data with natural heterogeneity in cloud conditions this result is therefore very acceptable.

It was furthermore tested to derive all classifiers on a  $9 \times 9$  (approx. similar area as in [WATANABE et al. 2016](#)),  $19 \times 19$ , or  $29 \times 29$  pixel subset. Most classifiers remain very similar. Only the classifiers ‘number of clouds’ and ‘cloud/cloud free changes are increasing in larger windows – which is obviously expected if using a larger window. The accuracy of classification is better for the  $29 \times 29$  pixel area. For the hourly mean classification the accuracy versus the reference database is 87, 90, and 92 % for the  $9 \times 9$ ,  $19 \times 19$ , and the  $29 \times 29$  pixel subset, respectively.

Therefore, all classifiers are from now on derived from a  $29 \times 29$  pixel cloud mask subset resulting in a classification accuracy of 92 %. This setting is also in line with findings from cloud type detection by [EBERT \(1987\)](#). They use  $32 \times 32$  AVHRR GAC pixels which is the same km pixel range as  $29 \times 29$  MSG SEVIRI pixels as each AVHRR GAC pixel is about  $3 \times 5 \text{ km}^2$  large.

### 3.4 Visual assessment of the satellite-based classification

The automatic satellite-based classification result was visually assessed for DNI time series measured at EnrMENA stations Adrar, Cairo, Erfoud, Missouri, Oujda, TanTan, and Zagora; BSRN stations Camborne, Carpentras, Payerne, Sede Boker; and DLR’s PSA station for the year 2012. The 1 min resolved ground observations of DNI were plotted as a time series with the corresponding satellite-based class coded as background colour inside each hour. Classification errors were identified visually and analysed by comparing these situations with colour composites of SEVIRI data to interpret the meteorological and geographical conditions.

Restrictions were found in regions with orographically induced clouds as e.g. at the Plataforma Solar de Almeria (PSA, Spain) where clouds are frequently caused by surrounding mountains. Such clouds are not representative for the PSA, which is located in the valley between the mountains. Especially, for PSA a frequent selection of class 3 with high DNI but some variability was observed in clear sky situations with low DNI variability. The same effect is observed in Carpentras in the case of fog in the surroundings.

The algorithm is sensitive to clouds only. Thin cirrus clouds can typically be detected due to the satellite’s infrared channels and the situation will be correctly identified as a non-clear variability class. On the other hand, atmospheric aerosols typically have a similar magnitude of DNI extinction and will result in a variability class 2 in ground-based DNI observations. But as the cloud retrieval is made to not detect aerosols, our method may overlook such DNI situations. This can be observed in stations as e.g. Adrar (Algeria) which are affected by desert dust.

Optically thin, low level clouds over deserts may be overlooked as well in the cloud masking, resulting in a clear-sky assumption, while the DNI would be classified as class 2 or 3. This is observed in many cases e.g. in Cairo with optically thin low-level clouds coming in from the ocean. During their solution over the warm land and therefore during their optically thinning process, they are still visible by the DNI ground observation as a small variability, but not by the satellite image anymore.

## 4 Example classification

As an illustration of classification results, the method is applied for 2012 at four BSRN stations located in Carpentras (France), Cabauw (The Netherlands), Sariguen (the station name is CENER, Spain), and Izana (Canary Islands, Spain). Fig. 8 illustrates the frequency histogram of irradiance variability classes for hourly daytime satellite-based cloud observations (top) as well as derived from ground-based DNI observations as discussed in SCHROEDTER-HOMSCHEIDT et al. (2018). Daytime hours are defined by a minimum solar elevation angle of 5° for the whole hour.

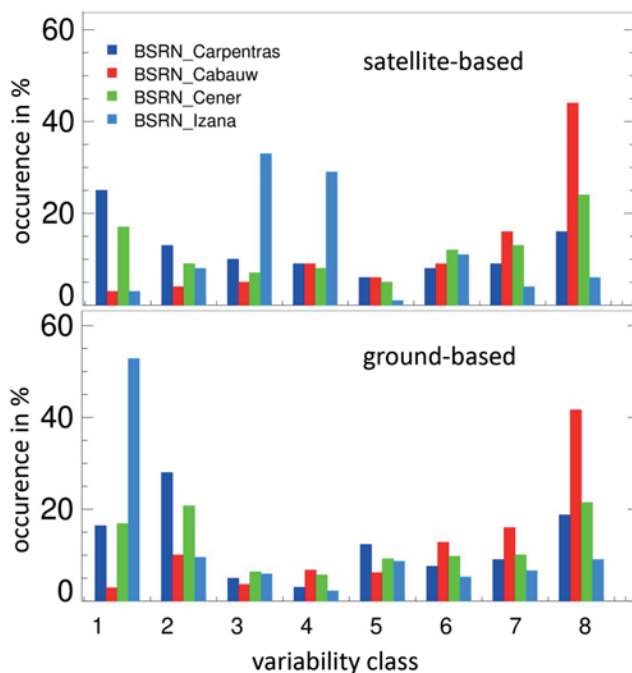


**Figure 8:** Comparison of classification results as obtained from satellite and ground-based observations at 4 BSRN stations and the year 2012.

In order to interpret the classification results, Fig. 9 describes the stations Carpentras, Cabauw, and Sariguen (CENER) with respect to the relative frequency of clear sky index  $k_c$  and beam clear sky index  $k_{cDNI}$  as well as the relative frequency of their increments in 1 min temporal resolution. The station Izana is omitted due to restrictions in the satellite-based classification as discussed below.

Carpentras has a maximum occurrence in variability classes 1 and 2, but also in class 8. The satellite-based classification identifies more often class 1 than class 2, while the ground-based classification derives 15 % more class 2 cases than class 1 results. Counting both classes together results in 38 % and 44 % for the satellite-based and the ground-based classification, respectively. Classes 3 and 4 are detected more often in the satellite-based classification than from ground, while the ground-based classification retrieves more often class 5. Especially, class 3 identification can be attributed to low cloud/fog situations in the surroundings. For classes 6, 7, and 8 the results are very similar. Overall, the low variability classes 1, 2, 5, and 8 are dominating in Carpentras, which explains the smaller  $k_c$  and  $k_{cDNI}$  increments observed in the annual statistics (Fig. 9, upper row).

For Cabauw as Northern station, variability classes 4, 6, 7, and 8 occur more frequently. Classes 1 and 2 are very rare. The estimates of satellite- and ground-based classifications are very similar with deviations below 2 % for classes 1, 3, 4, 5, 7, and 8; while classes 2 and 6 are classified 6 and 4 % more frequently by the ground-based methods.

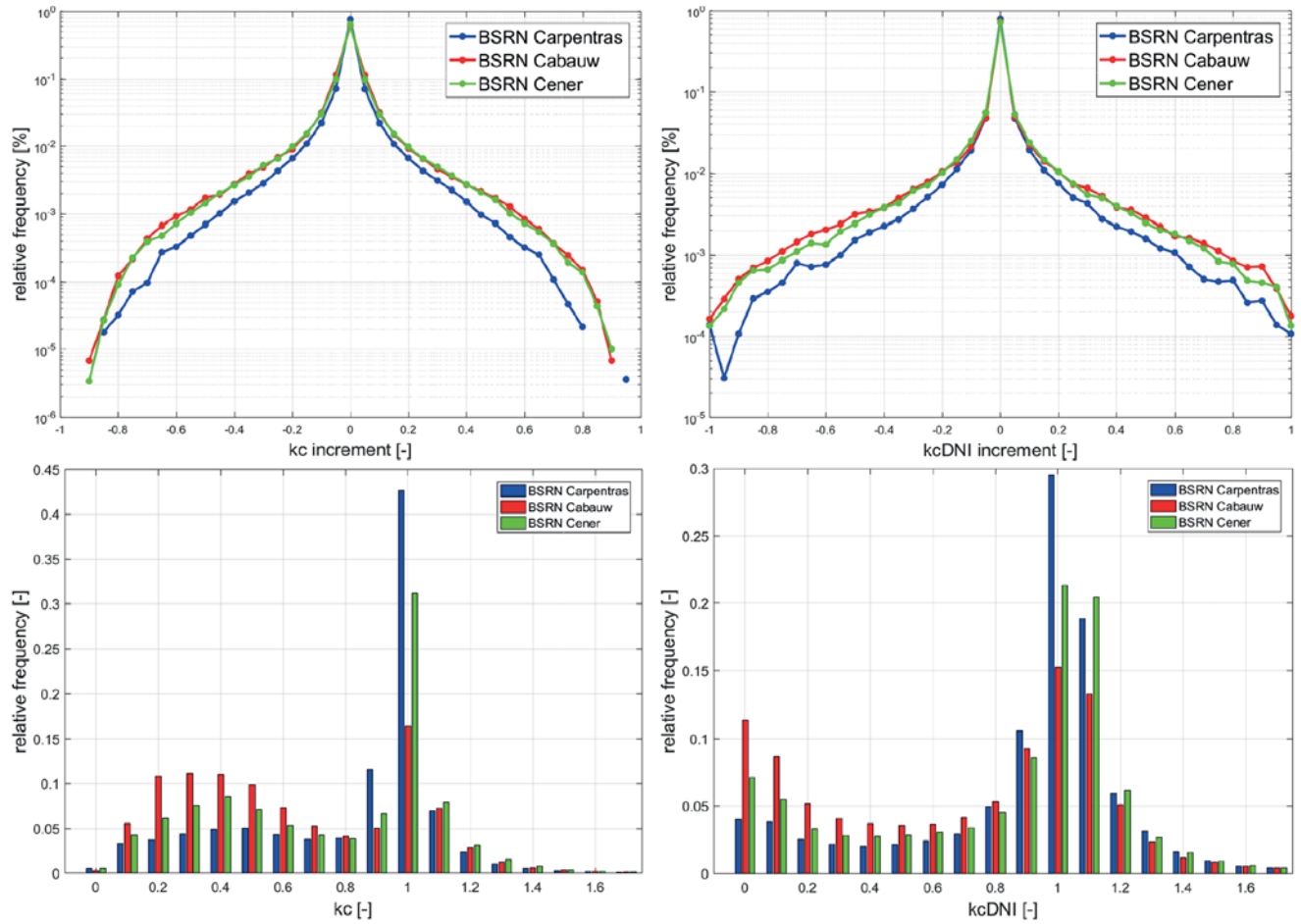


**Figure 9:** Relative frequency of  $k_c$  and  $k_{cDNI}$  increments observed in 1 min resolved ground observations (upper row) for the year 2012 – together with relative frequency distributions of  $k_c$  and  $k_{cDNI}$  itself.

CENER shows a similar pattern as Carpentras, but with less classes 1 and 2 and more frequent classes 6 to 8. The variable classes 4 and 6 are frequent. As for Carpentras and Cabauw, the occurrence of class 2 is underestimated compared to the ground-based classification by  $-12\%$ .

Cabauw and CENER stations show a very similar pattern in  $k_c$  and  $k_{cDNI}$  increments with larger increments both for global and direct irradiances than the station Carpentras. This reflects the larger occurrence of classes with higher variability. Nevertheless, the variability class distribution looks very different for both stations, while the increment statistics are very similar. This can be explained by the overall statistics of  $k_c$  and  $k_{cDNI}$  as given in Fig. 9 (lower row). Cabauw has a higher occurrence of cloudy skies with low  $k_c$  and  $k_{cDNI}$  values which is consistent with a larger occurrence of variability classes 6, 7, and 8. CENER on the other hand has a higher occurrence of clear skies with large  $k_c$  and  $k_{cDNI}$  which is reflected by a larger occurrence of variability classes 1 and 2 than Cabauw.

Overall, it can be seen that variability class 2 is chosen much more frequently by the ground-based classification scheme than by the satellite-based classification.

The latter prefers either class 1 or class 3 in such cases. As discussed in Section 3.2, in the satellite-based classification the discrimination of classes 1 to 4 is done only by the adjacent cloud situation while the actual satellite including the ground observation is retrieved by the satellite as cloud-free. Furthermore, any influence by aerosols is not considered. On the other hand, the ground-based classification uses the time series of DNI at the ground observation as information source. So, inaccuracies are expected, and it is overall interesting to see that the lower classification rate of class 2 is consistent at Carpentras, Cabauw, and CENER.

Izana is located in a unique geographical situation as a mountaintop station on an island. In this region often surrounding clouds occur above the ocean area while the station itself lies mostly in cloud-free conditions. Therefore, the classification result with large frequency of classes 3 and 4 based on the satellite classification and the large frequency of class 1 by the ground-based classification is expected. Class 1 is underestimated by  $50\%$  and classes 3 and 4 are overestimated by  $27\%$  each compared to the ground-based classification. Izana is a station illustrating the effect of non-representativeness of surrounding cloud structures for a specific location.

Similar overestimation of class 3 was found in the visual interpretation in Section 3.4 for the stations PSA due to convective clouds over surrounding mountains compared to the station located in a valley being often without these clouds.

## 5 Conclusions

A new automatic detection scheme of 1 min resolved surface solar irradiance variability classes from satellite-based cloud physical properties is presented. The method evaluates the surroundings of a location to describe the actual cloud situation and its impact on irradiance variability. The method provides an estimate of variability classes, which are each described by previously suggested variability metrics (SCHROEDTER-HOMSCHEIDT et al., 2018). The variability classes are also characterized with respect to direct normal and global horizontal irradiances in SCHROEDTER-HOMSCHEIDT et al. (2018). Therefore, the method is capable to describe various characteristics of irradiance variability being of interest for different user groups.

Multi-spectral cloud retrieval methods are applied in the satellite-based cloud retrieval scheme APOLLO (SAUNDERS and KRIEBEL, 1988; KRIEBEL et al., 2003). APOLLO is used to derive cloud physical parameters from Meteosat Second Generation (MSG) satellites. This database starts in February 2004 and is available for Europe, Africa, the Middle East and parts of Brasilia.

Additionally, satellite-based textural features are added as classifiers in the automatic classification scheme. They describe spatial cloud structures. These classifiers are selected and developed with focus on the needs of solar energy users for the detection of ramping irradiance conditions in either global or direct irradiances.

Textural features are derived from a group of pixels around the location of interest and cover a wider geographical region. Such classifiers are therefore less sensitive to parallax errors within the window, which are caused by solar viewing geometry and cloud height in single pixel classifiers. They may even take clouds into account which are overlooked in a single-pixel assessment due to the parallax error. On the other hand, textural features may cover a too large region to be representative for the pin-point like variability at the location of interest. Both effects are observed and cause individual misclassification in some satellite images.

Restrictions in classification accuracy are observed in cases with clouds in the surroundings which are not moving horizontally as e.g. static convective clouds forming above nearby mountains or steady fog in nearby regions. In such cases the spatial representativity as basic assumption of the method is not valid anymore. It will be investigated to detect such cases from the temporal variability from one cloud mask to the next cloud mask. Furthermore, the method is only sensitive to clouds and may overlook variability as introduced by aerosols in desertic regions.

It is obvious that exact irradiance observation at a single point is not accessible from space-borne sensors with a much lower spatial and temporal resolution, but the aim of this study is to assess the type of variability rather than to quantify each 1 min value exactly.

Time series of irradiance variability classes can be derived from 2004 onwards at each location of interest in Europe, Africa, and the Middle East. They have been used in extended site auditing for several test cases (e.g. SCHROEDTER-HOMSCHEIDT et al., 2016; SCHRECK, 2018; NOURI et al., 2019). Similar satellite-based capacities became available in recent years for Asia and for the Americas with the Himawari and GOES-16/-17 satellites.

Based on the satellite temporal resolution of 15 or even 5 min in the rapid scanning mode, several consecutive estimates of the irradiance variability class inside each hour are feasible. Several strategies are possible in the future development and application of the method: use of a moving hourly estimate over time with updates every 5 or 15 min, monitoring of the stability of the variability class identification inside the hour of interest, or the integration of the temporal variability of cloud statistical parameters itself as a classifier in the irradiance variability classification.

NOURI et al. (2019) showed how a DNI variability classification can be used to assess a method's uncertainty systematically. Classifying variability classes for a historical time series at any location can help to estimate the uncertainty of a forecast scheme for the location of interest depending on the typical cloud patterns and variability classes. NOURI et al. (2019) applied it for a sky camera based nowcasting system, but the same principle can be applied to any numerical weather prediction based solar irradiance forecast or to any other method to retrieve solar irradiance data.

The variability classes may furthermore be suitable to derive efficiency factors for renewable energy technologies. They can be used for the power output calculations of both photovoltaic and concentrating solar thermal power plants for each irradiance variability class separately. Or they can be used to derive life time correction factors for storage systems – quantifying the effect that a larger percentage of highly variable conditions at a location will reduce the system's life time.

The automatic characterization of each hour may avoid the need for a system simulation in a temporal resolution of 1 min which is computationally costly and may not exist in all simulation software packages already. Replacing nowadays hourly irradiance time series values by modified irradiance values, taking additionally into account the variability effects is currently under investigation.

The knowledge of variability classes at a location together with their properties can also be used to derive synthetic 1 min resolved time series with an artificial 1 min variability. Previous studies using Markov processes to derive global irradiance time series were e.g. based on daily clearness index (NGOKO et al., 2014) or

long-term meteorological parameters as sea level pressure, wind speed, cloud base height, and cloud cover (BRIGHT et al., 2015). A similar approach based on the spatial cloud features used in this study was tested (SCHRECK, 2018). This results in realistic time series for each meteorological situation and each point in a time series – and not just in a time series created from statistical mean properties only.

For several textural features a conditional suitability as classifiers were found as e.g. the number of cloud/cloud-free changes which is relevant only if there are a few clouds in the surroundings of a location. These findings are currently combined in the decision tree for the cloud area type but this finding of conditional suitability may be elaborated further in future.

Changes in cloud masks from one image to another image are also not yet included in the classifiers. Any cloud motion vector may serve as additional classifier on the horizontal replacement of the clouds – causing variability just by passing by while not changing the cloud shape necessarily as well. Nevertheless, this ‘frozen atmosphere’ assumption is often not valid in situations with convective clouds causing high variability cases. The value of such classifiers derived from consecutive images needs to be evaluated in future as well.

Furthermore, the approach will be tested for spatially higher resolved satellite imagery as provided by the Meteosat Third Generation satellites.

## Acknowledgements

The authors would like to thank the personnel from the BSRN, EnerMENA, and PSA stations. The study received support from the DNICast project (grant agreement no. 608623) within European Union’s Seventh Programme for research, technological development and demonstration as well as from the PreFlexMS project (grant agreement 654984) within European Union’s Horizon 2020 programme. Funding for validating and completing this research was further provided by the integrated project MetPVNet, project number 0350009A, financed by the Federal Ministry for Economic Affairs and Energy, Germany.

## References

ANVARI, M., G. LOHMANN, M. WÄCHTER, P. MILAN, E. LORENZ, D. HEINEMANN, M. REZA RAHIMI TABAR, J. PEINKE, 2016: Short term fluctuations of wind and solar power systems. – *New J. Phys.* **18**, 063027, DOI:10.1088/1367-2630/18/6/063027.

BERENDES, T.A., J.R. MECIKALSKI, W.M. JR. MACKENZIE, K.M. BEDKA, U.S. NAIR, 2008: Convective cloud identification and classification in daytime satellite imagery using standard deviation limited adaptive clustering. – *J. Geophys. Res.* **113**, D0207, DOI:10.1029/2008JD10287.

BEYER, H.G., A. HAMMER, J. LUTHER, J. POPLAWSKA, K. STOLZENBURG, P. WIETING, 1994: Analysis and synthesis of cloud pattern for radiation field studies. – *Sol. Energy* **52**, 379–390, DOI:10.1016/0038-092X(94)90115-I.

BORG, E., B. FICHELTMANN, H. ASCHE, 2011: Assessment for Remote Sensing Data: Accuracy of Interactive Data Quality Interpretation. – In: MURGANTE, B. et al. (Eds), The International conference on Computational Science and its Applications (ICCSA) 2011, Part II. – Lecture Notes in Computer Science (LNCS) **6783**, 366–375.

BRIGHT, J.M., C.J. SMITH, P.G. TAYLOR, R. CROOK, 2015: Stochastic generation of synthetic minutely irradiance time series derived from mean hourly weather observation data. – *Sol. Energy* **115**, 229–242. ISSN 0038-092X, DOI:10.1016/j.solener.2015.02.032.

CARVALHO, L.M.V., M.A.F. SILVA DIAS, 1998: An Application of Fractal Box Dimension to the Recognition of Mesoscale Cloud Patterns in Infrared Satellite Images. – *J. Appl. Meteor.* **37**, 1265–1282, DOI:10.1175/1520-0450(1998)037<1265:AAOFBD>2.0.CO;2.

EBERT, E., 1987: A pattern recognition technique for distinguishing surface and cloud types in the polar regions. – *J. Climate Appl. Meteor.* **26**, 1412–1427, DOI:10.1175/1520-0450(1987)026<1412:APRTFD>2.0.CO;2.

ELSINGA, B., W.G., J.H.M. VAN SARK, 2017: Analytic model for correlations of cloud induced fluctuations of clear-sky index. – *Sol. Energy* **155**, 985–1001, DOI:10.1016/j.solener.2017.07.035.

FERNÁNDEZ-PERUCHENA, C.M., A. BERNARDOS, 2015: A comparison of one-minute probability density distributions of global horizontal solar irradiance conditioned to the optical air mass and hourly averages in different climate zones. – *Sol. Energy* **112**, 425–436, DOI:10.1016/j.solener.2014.11.030.

GARAND, L., 1988: Automated recognition of oceanic cloud patterns. Part I: Methodology and application to cloud climatology. – *J. Climate* **1**, 20–39, DOI:10.1175/1520-0442(1988)001<0020:AROCCP>2.0.CO;2.

GLAS, S., 2014: Analysis of the Relation between Spatial Cloud Patterns in Satellite Images and Variability as seen in High-Resolution Irradiance Time Series by means of their Daily Profile Categorization. – Bachelor thesis, Hochschule für Angewandte Wissenschaften, München, Germany.

GSCHWIND, B., L. WALD, P. BLANC, M. LEFÈVRE, M. SCHROEDTER-HOMSCHIEDT, A. AROLA, 2019: Improving the McClear model estimating the downwelling solar radiation at ground level in cloud-free conditions – McClear-v3. – *Meteorol. Z.* **28**, 2, 147–163, DOI:10.1127/metz/2019/0946.

HINKELMAN, L.M., A. HEIDINGER, M. SENGUPTA, A. HABTE, 2013: Relating solar resource variability to cloud type. – ASES National Solar Conference, April 2013, Baltimore, Maryland, USA.

HOFF, T.E., R. PEREZ, 2012: Modeling PV fleet output variability. – *Sol. Energy* **86**, 2177–2189, DOI:10.1016/j.solener.2011.11.005.

IQBAL, M., 1983: An Introduction to Solar Radiation. – Academic Press, Canada.

JAKOB, C., G. TSELILOUDIS, 2003: Objective identification of cloud regimes in the Tropical Western Pacific. – *Geophys. Res. Lett.* **30**, 21, DOI:10.1029/2003GL018367.

JUNG, S., 2015: Variabilität der solaren Einstrahlung in 1-Minuten aufgelösten Strahlungszeitserien. – Master thesis, Universität Augsburg, Germany.

KANG, B.O., K.-S. TAM, 2013: A new characterization and classification method for daily sky conditions based on ground-based solar irradiance measurement data. – *Sol. Energy* **94**, 102–118, DOI:10.1016/j.solener.2013.04.007.

KATO, T., T. INOUE, Y. SUZUOKI, 2011: Estimation of Total Power Output Fluctuation of High Penetration Photovoltaic Power Generation System. – in Proc. IEEE Power and Energy Society General Meeting, Detroit, USA, DOI:10.1109/PES.2011.6039560.

- KRIEBEL, K.T., R.W. SAUNDERS, G. GESELL, 1989: Optical Properties of Clouds Derived from Fully Cloudy AVHRR Pixels. – *Beitr. Phys. Atmos.* **62**, 165–171, DOI: [oai:elib.dlr.de:64671](https://doi.org/10.1016/j.solener.2011.06.031).
- KRIEBEL, K.T., G. GESELL, M. KÄSTNER, H. MANNSTEIN, 2003: The cloud analysis tool APOLLO: Improvements and Validation. – *Int. J. Rem. Sens.* **24**, 2389–2408, DOI: [10.1080/01431160210163065](https://doi.org/10.1080/01431160210163065).
- LAVE, M., J. KLEISSL, E. ARIAS-CASTRO, 2012: High-frequency irradiance fluctuations and geographic smoothing. – *Sol. Energy* **86**, 2190–2199, DOI: [10.1016/j.solener.2011.06.031](https://doi.org/10.1016/j.solener.2011.06.031).
- LEFÉVRE, M., A. OUMBE, P. BLANC, B. ESPINAR, B. GSCHWIND, Z. QU, L. WALD, M. SCHROEDTER-HOMSCHIEDT, C. HOYER-KLICK, A. AROLA, A. BENEDETTI, J.W. KAISER, J.-J. MORCETTE, 2013: McClear: a new model estimating downwelling solar radiation at ground level in clear-sky conditions. – *Atmos. Meas. Tech.* **6**, 2403–2418, DOI: [10.5194/amt-6-2403-2013](https://doi.org/10.5194/amt-6-2403-2013).
- LONG, C.N., E.G. DUTTON, 2012: BSRN Global Network recommended QC tests, V2.0. – Document accessible via [http://www.bsrn.awi.de/fileadmin/user\\_upload/Home/Publications/BSRN\\_recommended\\_QC\\_tests\\_V2.pdf](http://www.bsrn.awi.de/fileadmin/user_upload/Home/Publications/BSRN_recommended_QC_tests_V2.pdf).
- MAAFI, A., S. HARROUNI, 2003: Preliminary results of the fractal classification of daily solar irradiances. – *Sol. Energy* **75**, 53–61, DOI: [10.1016/S0038-092X\(03\)00192-0](https://doi.org/10.1016/S0038-092X(03)00192-0).
- OHMURA, A., E.G. DUTTON, B. FORGAN, C. FRÖHLICH, H. GALEN, H. HEGNER, A. HEIMO, G. KÖNIG-LANGLO, B. MCARTHUR, G. MÜLLER, R. PHILIPONA, R. PINKER, C.H. WHITLOCK, K. DEHNE, 1998: Baseline Surface Radiation Network (BSRN/WCRP): New Precision Radiometry for Climate Research. – *Bull. Amer. Meteor. Soc.* **79**, 2115–2136, DOI: [10.1175/1520-0477\(1998\)079<2115:BSRNBW>2.0.CO;2](https://doi.org/10.1175/1520-0477(1998)079<2115:BSRNBW>2.0.CO;2).
- NGOKO, B.O., H. SUGIHARA, T. FUNAKI, 2014: Synthetic generation of high temporal resolution solar radiation data using Markov models. – *Sol. Energy* **103**, 160–170, ISSN 0038-092X, DOI: [10.1016/j.solener.2014.02.026](https://doi.org/10.1016/j.solener.2014.02.026).
- NOURI, B., S. WILBERT, P. KUHN, N. HANRIEDER, M. SCHROEDTER-HOMSCHIEDT, A. KAZANTZIDIS, L. ZARZALEJO, P. BLANC, S. KUMAR, N. GOSWAMI, R. SHANKAR, R. AFFOLTER, R. PITZ-PAAL, 2019: Real-Time Uncertainty Specification of All Sky Imager Derived Irradiance Nowcasts. – *Remote Sens.* **11**, DOI: [10.3390/rs11091059](https://doi.org/10.3390/rs11091059).
- PEREZ, R., S. KIVALOV, J. SCHLEMMER, K. JR. HEMKER, T. HOFF, 2011: Parameterization of site-specific short-term irradiance variability. – *Sol. Energy* **85**, 1343–1353, DOI: [10.1016/j.solener.2011.03.016](https://doi.org/10.1016/j.solener.2011.03.016).
- PIETRAPERTOSA, C., V. CUOMO, N. PERGOLA, C. SERIO, V. TRAMUTOLI, H. SHIMODA, 2001: Fractality in broken clouds and the scan geometry of new satelliteborne infrared sensors. – *Int. J. Rem. Sens.* **22**, 889–894, DOI: [10.1080/01431160051060381](https://doi.org/10.1080/01431160051060381).
- RAUSCHER, T., 2013: Application of Mathematical and Communicational Methods for Characterisation of Diurnal Global Horizontal Irradiance Variations and Categorization of Daily Profiles. – Bachelor Thesis ID number 741, Munich University of Applied Sciences.
- RENO, M.J., J.S. STEIN, 2013: Using cloud classification to model solar variability. – ASES National Solar conference, April 2013, Baltimore, Maryland.
- SAUNDERS, R.W., K.T. KRIEBEL, 1988: An improved method for detecting clear sky and cloudy radiances from AVHRR data. – *Int. J. Rem. Sens.* **9**, 123–150, DOI: [10.1080/01431168808954841](https://doi.org/10.1080/01431168808954841).
- SCHADE, N.H., A. MACKE, H. SANDMANN, C. STICK, 2007: Enhanced solar global irradiance during cloudy sky conditions. – *Meteorol. Z.* **16**, 295–303, DOI: [10.1127/0941-2948/2007/0206](https://doi.org/10.1127/0941-2948/2007/0206).
- SCHRECK, S., 2018: Implications of Sub-Hourly Solar Radiation Variability on Decentralized Energy Systems. – Master thesis, Universität Stuttgart, Germany.
- SCHROEDTER-HOMSCHIEDT, M., M. KOSMALE, J.L. CASADO RUBIO, C.M. FERNANDEZ PERUCHENA, L. GUERREIRO, 2016: Validation sites, deliverable D4.2. – EU H2020 project Pre-FlexMS, public report.
- SCHROEDTER-HOMSCHIEDT, M., S. JUNG, M. KOSMALE, 2018: Classifying ground-measured 1 minute temporal variability within hourly intervals for direct normal irradiances. – *Meteorol. Z.* **27**, 160–179, DOI: [10.1127/metz/2018/0875](https://doi.org/10.1127/metz/2018/0875).
- SCHÜLER, D., S. WILBERT, N. GEUDER, R. AFFOLTER, F. WOLFERTSTETTER, C. PRAHL, M. RÖGER, M. SCHROEDTER-HOMSCHIEDT, G. ABDELLATIF, A. ALLAH GUIZANI, M. BALTHOUTHI, A. KHALIL, A. MEZRHAB, A. AL-SALAYMEH, N. YASSAA, F. CHELLALI, D. DRAOU, P. BLANC, J. DUBRANNA, O.M.K. SABRY, 2016: The enerMENA Meteorological network – Solar Radiation Measurements in the MENA Region, AIP Conference Proceedings, 1734, 150008, DOI: [10.1063/1.4949240](https://doi.org/10.1063/1.4949240).
- SKARTVEIT, A., J.A. OLSETH, 1992: The probability density and autocorrelation of short-term global and beam irradiance. – *Sol. Energy* **49**, 6, 477–487, DOI: [10.1016/0038-092X\(92\)90155-4](https://doi.org/10.1016/0038-092X(92)90155-4).
- TOMSON, T., 2010: Fast dynamic processes of solar radiation. – *Sol. Energy* **84**, 318–323, DOI: [10.1016/j.solener.2009.11.013](https://doi.org/10.1016/j.solener.2009.11.013).
- TOVAR, J., F.J. OLMO, F.J. BATLLES, L. ALADOS-ARBOLEDAS, 2001: Dependence of one-minute global irradiance probability density distributions on hourly irradiation. – *Energy* **26**, 659–668, DOI: [10.1016/S0360-5442\(01\)00024-X](https://doi.org/10.1016/S0360-5442(01)00024-X).
- WATANABE, T., Y. OISHI, T.Y. NAKAJIMA, 2016: Characterization of surface solar-irradiance variability using cloud properties based on satellite observations. – *Sol. Energy* **140**, 83–92, DOI: [10.1016/j.solener.2016.10.049](https://doi.org/10.1016/j.solener.2016.10.049).